

# A New Kinetic Monte Carlo Algorithm for Heteroepitactical Growth: Case Study of C<sub>60</sub> Growth on Pentacene

Rebecca A. Cantrell and Paulette Clancy\*

Department of Chemical and Biomolecular Engineering, Cornell University, Ithaca, New York 14853, United States

## S Supporting Information

**ABSTRACT:** A novel multilattice kinetic Monte Carlo algorithm is developed for heteroepitactical growth of a hexagonal lattice material (C<sub>60</sub>) on an oblique lattice material (pentacene). This algorithm captures the behavior of single molecule and small clusters of C<sub>60</sub> molecules diffusing, clustering, and reorganizing as monolayers on the surface and switching lattices depending on their local environment. An extensive catalog of jump rates and energy barriers created from molecular dynamics simulations and molecular mechanics is used as the sole input to the method in order to follow the evolution of C<sub>60</sub> growth on pentacene for time scales approaching a millisecond that are unattainable using molecular dynamics alone.

## 1. INTRODUCTION

In several previous papers,<sup>1–4</sup> we have explored the structural properties of a system containing C<sub>60</sub> on pentacene, which is under current scrutiny as a prototypical p–n heterointerface for all-organic solar cells. The typically small exciton diffusion lengths in organic photovoltaic devices only allow electron–hole splitting if the excitons are formed very near or at the p–n junction interface. Since charge transport is related to structural orientational preferences, it is important to know the atomic-scale details of the interface between p- and n-type materials as a means to understand the performance of organic semiconductor materials.

The C<sub>60</sub>/pentacene heterojunction presented here describes a “planar heterojunction,” rather than a “bulk heterojunction”; the distinction being that bulk heterojunctions involve an interpenetrating blend of donor and acceptor molecules in an attempt to reduce the distance that an exciton has to travel to dissociate. Bulk heterojunctions can lead to a large charge recombination rate for the C<sub>60</sub>/pentacene pair,<sup>5</sup> while planar interfaces have a comparatively reduced contact area, diminishing the opportunity for excitons to dissociate. We chose to focus on a planar interface since the small lengthscales accessible in molecular simulations are better represented by a planar interface. The ability to grow ordered planes of C<sub>60</sub> on top of a pentacene surface in an ideal layer-by-layer manner is not straightforward. Two-dimensional C<sub>60</sub> growth is preferred based on a rubric that links increased structural order to higher electron and hole mobilities. We have presented evidence to suggest that C<sub>60</sub> “dewets” an upright pentacene surface, which is an undesirable outcome since it leads to 3D growth. Although this question is not directly answered here, the development of a kinetic Monte Carlo (KMC) method that would allow the prediction of growth patterns of C<sub>60</sub> on pentacene is the first step toward allowing the question of dewetting and 3D growth to be explored.

Our past studies used a combination of molecular statics and molecular dynamics (MD) to gain detailed information regarding the potential energy surface experienced by C<sub>60</sub> molecules as they traverse the surfaces of the well characterized bulk and thin film polymorphs of pentacene. These two polymorphs prefer to pack with the long axis of the pentacene molecule

almost upright; the thin film phase is tilted 9° off the surface normal, whereas the bulk phase is oriented 23° off normal. However, there are several factors that limit the scope of MD simulations of the growth of C<sub>60</sub> molecules on pentacene. The main obstacle arises from computational efficiency; in practice, it is generally beyond the resources of MD to study more than a handful of C<sub>60</sub> molecules on a reasonably sized pentacene surface layer. The pentacene part of the system should, at minimum, consist of surface molecules allowed to move and an underlying monolayer of pentacene that is fixed in place. This constitutes a large number of pentacene molecules. For instance, our MD simulations of four or fewer C<sub>60</sub> molecules on a 40 × 30 Å pentacene surface (5 × 5 bulk phase pentacene unit cells) involves the consideration of 3600 pentacene atoms. A second major obstacle is the inability of MD to follow the dynamics of the system for long enough for the formation of even one monolayer of C<sub>60</sub> molecules. An appropriate time step for this system is around 1 fs, thus the simulation of just one nanosecond of time involves the solution of the equations of motion one million times, taking approximately a week of computation time for an appreciable number of atoms. Coarse graining the C<sub>60</sub> molecules to be represented by a sphere and the pentacene molecules to a rigid body with a suitable (2.7:1) aspect ratio is a possibility, but the effect of these assumptions cannot easily be assessed without comparison either to experimental results for growth characteristics or to an all-atom simulation benchmark. The combination of these factors means that, without at least the employment of massively parallel computing resources or perhaps accelerated methods,<sup>6–9</sup> MD simulations of thin film growth at anything close to experimental time scales is beyond the reach of MD techniques.

A KMC approach could, in principle, bridge the atomistic length and time scales of MD to more mesoscopic dimensions and hence to experimentally accessible regimes. On-lattice KMC is a well used technique to study thin film growth.<sup>10–15</sup> However, standard KMC codes are unsuitable for studies of the

Received: November 15, 2011

Published: January 19, 2012



growth of substance A on top of a dissimilar substance B characterized by a different crystal structure, a process known as heteroepitactic growth. This is the case in our test case study, the growth of  $C_{60}$  (whose bulk crystal habit adopts a hexagonal FCC lattice) on top of pentacene, which grows in a triclinic habit. Heteroepitactic growth is distinct from heteroepitaxy; the latter denotes the growth of molecules of type A on those of type B with the same crystal structure, for instance, the growth of Ge on Si.

There has been only one report of a KMC simulation of heteroepitactic growth.<sup>16</sup> In this study by Hoffmann, the environmental conditions of a CO molecule on a Pd(100) surface (e.g., different adsorption site geometries) determined which of the two lattices it adopted, the lattice characteristic of CO or that of Pd. However, in that system, the two dissimilar lattices are forced to match at the periodic boundary conditions (effectively changing the lattice parameters), which is not an approach used in this work. Our goal then is to produce a KMC code whose underlying rules seamlessly recognize which lattice is most appropriate for a given situation resulting from deposition or diffusion. This paper will describe one way that this task can be accomplished.

To create a new KMC algorithm to study heteroepitactic growth involves the following major tasks. The first task, described in Section 2, is to design a suitable multilattice framework for the KMC simulations. For the  $C_{60}$ -pentacene system of interest here, a suitable KMC code will have to allow consideration of five lattices (two for pentacene and three for  $C_{60}$ ) that an incoming particle has the choice to adopt; the need for five lattices is described in Section 2. Section 3 will describe the large collection of energy barriers that are needed to capture all the processes involved in thin film heteroepitaxial growth and hence obtain rates for the dynamic simulation. In Section 4, a few key parameters in the simulation have to be estimated, including the choice of prefactors for diffusion events and deposition rates. The paper concludes in Section 5 with sample test runs of the code for the thin film growth of  $C_{60}$  on pentacene, where intra- and interlayer diffusion is considered.

## 2. ALGORITHM DEVELOPMENT

In this section, we will describe the construction of a framework of multiple lattices and the main assumptions built into the code. KMC codes involve the consideration of “events,” defined as any action that has an associated rate; in this study, events include deposition, diffusion, and desorption. Diffusion events are referred to as “transitions,” where a  $C_{60}$  molecule physically transitions from occupying one lattice site to another. As shown in Figure 1, the basic KMC algorithm created to describe heteroepitactical growth begins by a random selection of an event (whether deposition, a diffusional transition, or a desorption event). The complexity of this algorithm lies in the handling of diffusional events; this is described in the next section.

**2.1. Q–P Lattice Development.** The motivation for the multiple-lattice structure of the new KMC code stemmed from the fact that  $C_{60}$  molecules behave differently when they are effectively alone on a pentacene surface (i.e., they have no  $C_{60}$  neighbors) in comparison to situations when they are near other  $C_{60}$  molecules on a pentacene surface. From our previous MD simulations,<sup>1</sup> it was clear that a single  $C_{60}$  molecule on the pentacene surface prefers to reside at certain locations relative to the pentacene positions, especially on bulk phase pentacene. The potential energy surface created by one  $C_{60}$  molecule experiencing bulk and thin film phases of pentacene was obtained

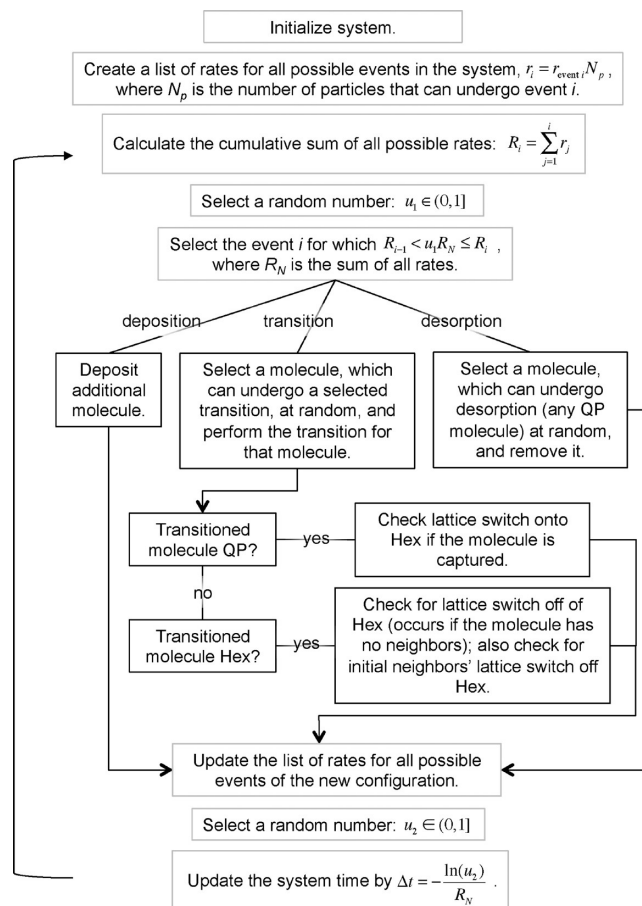


**Figure 1.** KMC algorithm implemented in this work employing a multilattice framework. The steps outlined in gray are the standard KMC steps, whereas those outlined in black show how the multilattice framework is implemented.

from our earlier studies; this provided the “blueprint” for the lattice points for the first monolayer of growth. Lattice point locations correspond to energy minima on the pentacene surface in the  $x$ – $y$  plane.<sup>2</sup> Figure 2 shows such a potential energy surface for a bulk phase pentacene surface. “Thin film” and “bulk” polymorphs of pentacene preferentially form a herringbone crystalline configuration, in which the corresponding potential energy surface (although periodic) is not a simple rectangular or hexagonal pattern. As we have shown previously,<sup>1</sup> there are important saddle points which are low-energy sites (i.e., preferential locations for  $C_{60}$  molecules). To describe this anisotropic surface, we developed a periodic lattice pattern incorporating these low-energy well locations as a function of the uppermost hydrogen positions of the upright pentacene molecules. There are four such hydrogen atoms, whose positions define one of the energy minima; we call this a quadrilateral “Q” site, representing the geometry of the energy minimum. There are five uppermost hydrogen atoms whose positions define the other energy minimum (the saddle point). We call this a pentagonal “P” site, reflecting the geometry of the energy minimum. Q and P sites cover the majority of the pentacene surface, and hence, we have defined the surface of pentacene as being represented as a set of P and Q sites, as shown in Figure 2.

A  $C_{60}$  molecule located at a Q site can move laterally in 12 different directions (6 to other Q sites and 6 to P sites). Similarly, a  $C_{60}$  molecule at a P site can move in 12 different

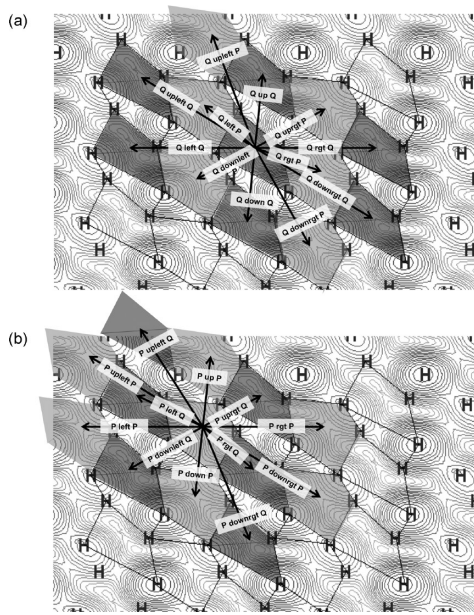


**Figure 2.** Q–P lattice system overlaid on a  $C_{60}$ /bulk pentacene potential energy surface. Darker gray quadrilateral shapes (Q sites) are defined by four specific uppermost pentacene hydrogen locations, and lighter gray pentagon shapes (P sites) are defined by five uppermost pentacene hydrogen locations. Possible transitions from Q-to-P and Q-to-Q sites are labeled in (a), and possible transitions from P-to-Q and P-to-P sites are labeled in (b). “Right” is shortened to “rgt” for simplicity.

directions (6 to Q sites and 6 to other P sites), as shown in Figure 2. Adoption of these Q and P lattices, while complicated, was necessary in order to capture the pronounced anisotropy observed in MD simulations of  $C_{60}$  diffusion on a bulk phase of pentacene, which is absent for the diffusion on the thin film phase.<sup>2</sup> One important test of the new KMC code will be to verify that it reproduces the diffusional anisotropy seen in MD simulations of a single probe  $C_{60}$  molecule. Following that, it will be interesting to determine if this anisotropy affects the shapes of  $C_{60}$  islands that form during thin film growth, as this information was inaccessible from the MD simulations. This will be addressed in Section 5.

**2.2. “Hex” Lattice Development.** With the Q and P lattices representing the pentacene surface, the next task is to determine which lattices are necessary to represent sites for  $C_{60}$  molecules when they are in the vicinity of other  $C_{60}$  molecules as they diffuse over a pentacene surface. The diffusion of  $C_{60}$  molecules is quite different near other  $C_{60}$  molecules than when they are isolated on the pentacene surface.<sup>1</sup>  $C_{60}$  molecules tend to remain an equilibrium distance ( $\sim 1$  nm) apart from other  $C_{60}$  molecules throughout nanosecond MD simulations of two, three, and four  $C_{60}$  molecules, the largest all-atom studies we were able to study. Small clusters of  $C_{60}$  molecules appear to be relatively oblivious to where they reside with respect to the pentacene surface as long as they can precess around their  $C_{60}$  neighbors. The main reason for this is the considerably stronger  $C_{60}$ – $C_{60}$  interaction compared to the interaction between  $C_{60}$  and the upright pentacene surface. Clustering of these roughly spherical molecules leads to a close-packed type lattice, indeed, that is the preferred crystal packing habit for  $C_{60}$ . To capture this in the KMC algorithm, we developed an additional lattice type representative of a hexagonal shape (a “Hex” lattice). During submonolayer growth, a  $C_{60}$  molecule on a Hex lattice

can move in six possible directions, which we have designated as: up-left, up-right, right, down-right, down-left, and left. Thus we have three characteristic lattices so far, Q, P, and Hex, to represent submonolayer growth, as shown in Figure 3a.

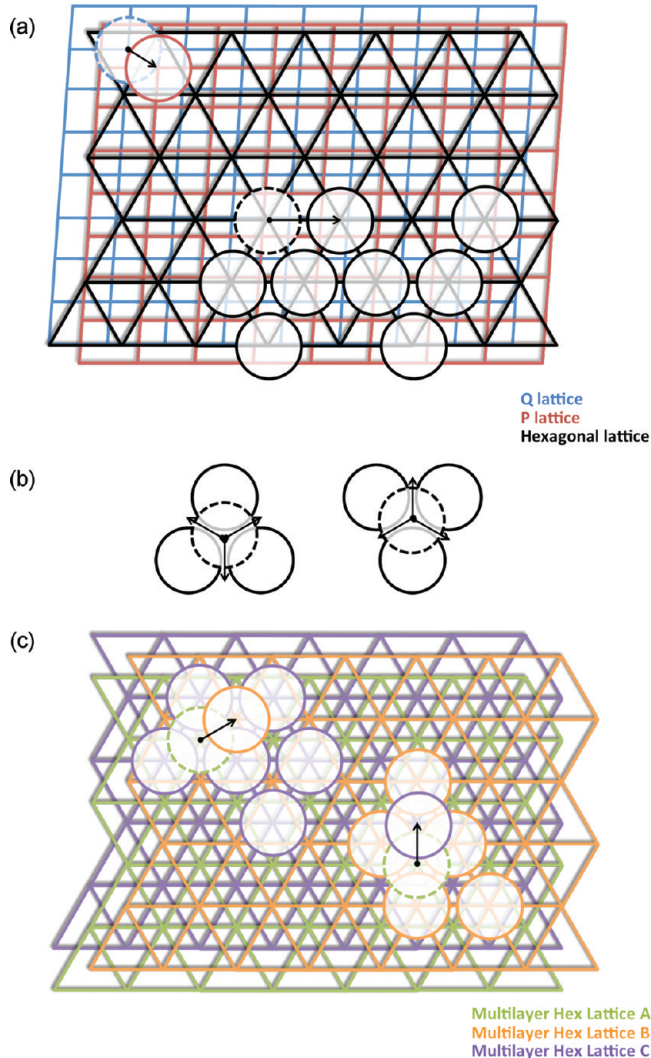


**Figure 3.** (a) Multilattice system used in the KMC algorithm to capture submonolayer diffusion of  $C_{60}$  on an upright pentacene phase. The Q (blue) and P (red) lattices correspond to sites of possible  $C_{60}$  residence when a  $C_{60}$  molecule is not in the vicinity of another  $C_{60}$  molecule. The Hex lattice (black) corresponds to sites of possible  $C_{60}$  residence when a  $C_{60}$  molecule is in the vicinity of at least one other  $C_{60}$  molecule. (b) Possible jump directions for  $C_{60}$  on  $C_{60}$ . (c) Multilattice system used in KMC for beyond monolayer diffusion of  $C_{60}$  on  $C_{60}$  with example diffusion events.

Growth beyond the first monolayer of  $C_{60}$  molecules is largely the same as the submonolayer Hex lattice, except that a  $C_{60}$  molecule in this situation can now only move in three possible directions, depending on whether it resides on top of an “upright”  $C_{60}$  triangle (possible directions: up-left, up-right, or down) or a “downward”  $C_{60}$  triangle (possible directions: up, down-right, or down-left), as shown in Figure 3b. Since  $C_{60}$  prefers to pack in an fcc lattice structure, there are three hexagonally close-packed planes, denoted as A, B, and C. The  $C_{60}$  plane (A, B, or C), underneath which another  $C_{60}$  is diffusing, determines its own designation (A, B, or C). Figure 3c shows a schematic example of the movements (or “jumps”)

of  $C_{60}$  molecules beyond the first monolayer. Submonolayer  $C_{60}$  molecules on a Hex lattice can also either be of type A, B, or C; for simplicity, this was not shown in Figure 3a. In total, there are five lattices that are needed: P, Q, Hex-A, Hex-B, and Hex-C.

**2.3. System Size.** The implementation of periodic boundary conditions in a multilattice simulation is not trivial. Matching the oblique shape of the Q and P lattices and the hexagonal Hex lattice at the boundary conditions could not, in practice, be achieved exactly. Figure 4 shows the periodic

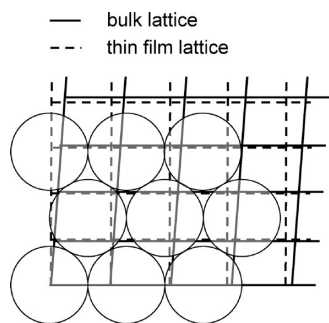


**Figure 4.** Diagram showing the incommensurability of the  $C_{60}$  Hex lattice with the oblique bulk pentacene lattice (solid lines) and thin film pentacene lattice (dashed lines). The overlaid  $C_{60}$  molecules are shown as circles, sized relative to the pentacene lattice parameters.

boundary incommensurability more clearly for both thin film and bulk phase polymorphs of pentacene. As an alternative to changing the lattice constants, we minimized the boundary mismatch. We defined “boundary mismatch” as the sum of the distances between the bottom left corner (where a lattice point resides at the origin) and the three other periodic lattice point images. We set the tolerance for the mismatch at a value of  $\sim 5 \text{ \AA}$ , which seemed appropriately small. Many large system sizes meet this tolerance, but the speed of the code depends sensitively on the number of particles, roughly as  $O(N)$ . Hence, it is important to constrain the total number of possible submonolayer particles (i.e., the system size). Lastly, we wanted a system size with a reasonable aspect ratio ( $>0.5$  and  $<2$ ) in order to minimize the amount of periodic boundary crossings in the simulation. For the system size, we started by considering

the number of  $C_{60}$  molecules that would fit on  $80 \times 80$  units cells of bulk pentacene (3528  $C_{60}$  molecules), since this seemed large enough to be representative of surface growth. Applying the criteria listed above (a reasonable aspect ratio and a periodic boundary mismatch within tolerance), we narrowed the possible choices of system sizes to a set of 15 for each of the bulk and thin film phase pentacene systems. Figure 5 shows the normalized values of these parameters for the bulk and thin film phase pentacene systems.

Using these criteria, the system size chosen for the bulk phase was  $71 \times 89$  pentacene unit cells for which the periodic boundary mismatch,  $\sum d_i = 3$ , the maximum number of submonolayer  $C_{60}$  molecules = 3483, and the aspect ratio of the system = 1.04. Similarly, the system size chosen for the thin film phase was  $52 \times 130$  pentacene unit cells for which the  $\sum d_i = 6$ , the maximum number of submonolayer  $C_{60}$  molecules = 3499, and the aspect ratio = 0.51. Finding an appropriate system size for the thin film phase was more difficult because the angle  $\gamma$  between lattice parameters  $a$  and  $b$  is almost  $90^\circ$ , making commensurate periodic system sizes harder to attain. The smaller aspect ratio for the thin film phase systems explains why subsequent KMC snapshots of this system are taller than their bulk phase counterparts.

**2.4. Algorithm Details and Assumptions.** Certain assumptions were made in the KMC code that are either inherent in the discrete nature of such codes or a result of practicality. First, all diffusion event rates depend only on temperature, that is, they are assumed to be activated events. The rates for Q–P jumps are obtained by collecting the frequencies of these events from many MD simulations (as described in Section 3.1). This method was infeasible for Hex lattice jumps (both submonolayer and beyond monolayer growth), since they are rare enough not to be observable on MD time scales, so their energy barriers were calculated statically and the attempt frequency, or Arrhenius prefactor, was assumed to be the average of the obtained prefactors from the Q–P jumps. The sensitivity of changing this prefactor for Hex lattice jumps is discussed in Section 4.

Second, a  $C_{60}$  “capture radius” was built into the KMC code and defined as a function of temperature. The capture radius is defined as the distance within which a  $C_{60}$  molecule will inevitably be captured by another  $C_{60}$  molecule, resulting in

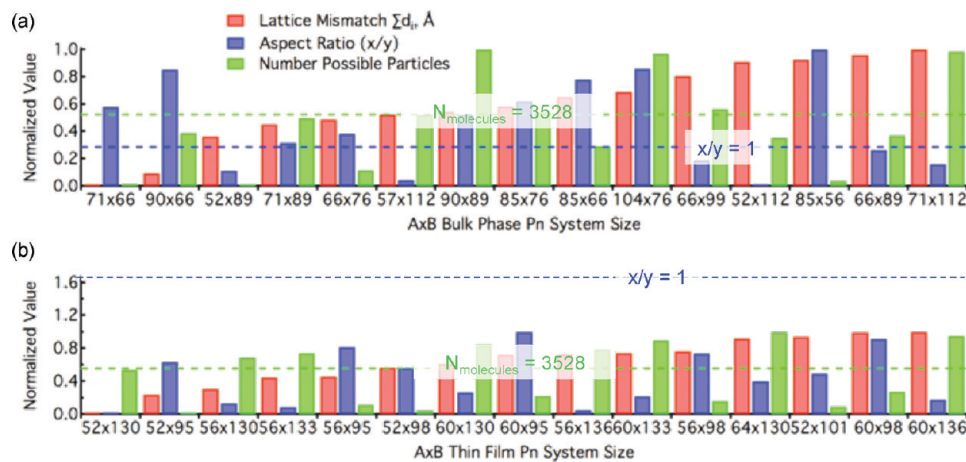


**Figure 5.** System size parameters: Periodic boundary mismatch ( $\sum d_i$  = sum of the distances between the bottom left corner, where a lattice point resides at the origin, and the three other periodic lattice point images), system aspect ratio, and maximum number of possible particles. The target lattice mismatch is zero, and the normalized target values for the other parameters are shown by the dotted green and blue lines for (a) bulk phase and (b) thin film phase pentacene.

either the captured  $C_{60}$  molecule joining an existing  $C_{60}$  cluster or forming a new cluster with another lone  $C_{60}$  molecule. The capture radius is calculated based on the inverse of the Pacheco intermolecular potential function between two  $C_{60}$  molecules.<sup>17</sup> At 0 K, the capture radius was set equal to the distance at which this potential energy function is minimized (i.e., the value of  $r$  at  $E_{\min}$ ). At higher temperatures, the capture radius was set equal to the distance ( $>r$  at  $E_{\min}$ ) at which the function is equal to  $E_{\min} + k_B T$ . Figure 6 shows the capture radius as a function of

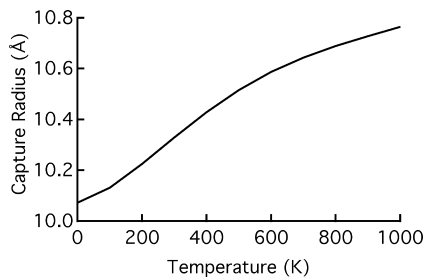


Figure 6. Dependence of capture radius on temperature.

temperature, which is relatively weak; increasing the temperature from 0–1000 K increases the capture radius by only 0.7 Å.

Simulating deposition events in the KMC code involves further assumptions. In the code, a deposition event involves the instantaneous appearance of a randomly placed molecule in the vacuum above the surface. In reality, this would be mostly analogous to a vapor phase deposition process in which the incident molecules do not carry any significant incident energy. If  $C_{60}$  deposition occurs on the pentacene surface, it joins the Q–P lattice first by default. If the deposition occurs very close to another  $C_{60}$  molecule, the deposited molecule either becomes an adjacent neighbor or resides atop if there is a triangle of  $C_{60}$  molecules beneath that would permit it, as shown in Figure 3b. One exception to this deposition protocol is the rare case when there is no appropriate lattice position for a deposited molecule, in which case the randomly located deposition is retried. An example would be deposition at a  $C_{60}$  grain boundary, where the molecule can neither roll off an edge nor be added to the monolayer. Another rare example would be a deposition at a lattice mismatched corner where the slight lattice shift confuses the placement of the deposited particle.

The range of accessible deposition rates in the code is much higher ( $10^4$ – $10^6$  ML/s) than is generally experimentally feasible ( $\sim 1$  ML/s). These high deposition rates are essentially dictated by the speed of KMC codes, so that the simulation does not take an impractically long time. For example, a simulation of  $C_{60}$  growth on  $71 \times 89$  pentacene unit cells takes approximately 2 weeks for a deposition rate of  $10^5$  ML/s on a single core AMD Opteron at 2.6 GHz CPU (or  $\sim 1.5$  weeks on an Intel Xeon core operating at 2.93 GHz). Increasing deposition rates for the sake of computational efficiency is often done in KMC because the rate of diffusion is much faster than deposition.<sup>18,19</sup> Thus, in order to follow the simulation of film growth progress as a function of time at a tractable elapsed “wall clock” time, the deposition rate had to be set high. Section 4 will describe the sensitivity of the results to deposition rate.

Desorption was also considered as a possible event in the KMC code, but it was only allowed for single  $C_{60}$  molecules on the Q–P lattice for several reasons. First, if a  $C_{60}$  molecule is connected to another  $C_{60}$  molecule on a Hex lattice, the admolecule–system interaction strength ( $>0.3$  eV, the  $C_{60}$ – $C_{60}$

interaction strength) is likely to be too large to cause desorption to occur at any experimentally relevant temperatures. Second, desorption events for single  $C_{60}$  molecules (as would be represented on the Q–P lattice) were seen in MD simulations at high temperatures. Desorption events for  $C_{60}$  molecules in the presence of other  $C_{60}$  molecules are unlikely events, which would have taken an enormously long time to observe in MD. For single  $C_{60}$  desorption events, there were very few data points available for desorption rate as a function of temperature, so a linear dependence was chosen for simplicity. Desorption does not occur for  $C_{60}$  until  $\sim 500$  K for bulk phase pentacene and until  $\sim 525$  K for thin film phase pentacene, as extrapolated from the MD data. The higher desorption temperature for  $C_{60}$  from the thin film phase is reasonable, considering that the average adsorption energy for  $C_{60}$  on bulk phase pentacene is about 0.02 eV higher (i.e., less attractive) than that on thin film phase.

### 3. DETERMINATION OF ENERGY BARRIERS

The determination and cataloguing of energy barriers is a critical component of a KMC simulation. In this section, the compilation of energy barriers and other related information is described in detail for the multilattice diffusion events. As a convention, for site-to-site hops, we refer to  $C_{60}$  diffusion events on pentacene on the Q–P lattice as “QP jumps.” Analogously,  $C_{60}$  diffusion events on pentacene on a Hex lattice will be referred to as “Hex-sub jumps” (referring to jumps at the submonolayer level), and  $C_{60}$  diffusion events on  $C_{60}$  will be referred to as “Hex-bulk jumps” (referring to jumps beyond the first monolayer, where  $C_{60}$  follows its bulk lattice structure). It should be noted here that both Hex-sub and Hex-bulk jumps can be of type A, B, or C, as depicted in Figure 3c.

**3.1. QP Jump Rates.** For the QP jumps, jump rates were obtained by calculating the frequencies of many different diffusion events during MD simulations of a single  $C_{60}$  molecule diffusing on pentacene at different temperatures; all the possible QP jumps considered are shown in Figure 2. The temperatures tested ranged from 200 to 600 K, in increments of 25 K, and each MD simulation was run for 2 ns. These sets of MD simulations were run for both the bulk and thin film phases of pentacene. The frequency vs temperature data were fitted to the Arrhenius equation, shown in eq 1, where  $v$  is the frequency of a jump,  $v_0$  is the attempt frequency,  $E_a$  is the activation energy,  $k$  is the Boltzmann constant, and  $T$  is the temperature. In cases where an Arrhenius fit was not appropriate, a second-order polynomial was fitted to the frequencies as a function of temperature.

Figures S1 and S2, Supporting Information show, respectively, the bulk and thin film phase frequencies as a function of temperature and the corresponding Arrhenius plot of the  $\ln(\text{frequency})$  versus  $1/k_B T$ . For linear Arrhenius plots with negative slope, we extracted energy barriers (slope) and pre-factors ( $y$ -intercept). In cases where the particular diffusion event is non-Arrhenian, the frequency was taken as a polynomial function of temperature. All of these data combined give temperature-dependent rates necessary for the submonolayer QP jumps in the KMC simulation.

$$v = v_0 e^{-E_a/kT} \quad (1)$$

**3.2. Verification of the QP Diffusion Aspects of the Code.** To verify the KMC model, the results of KMC-predicted diffusion were compared to those from an MD

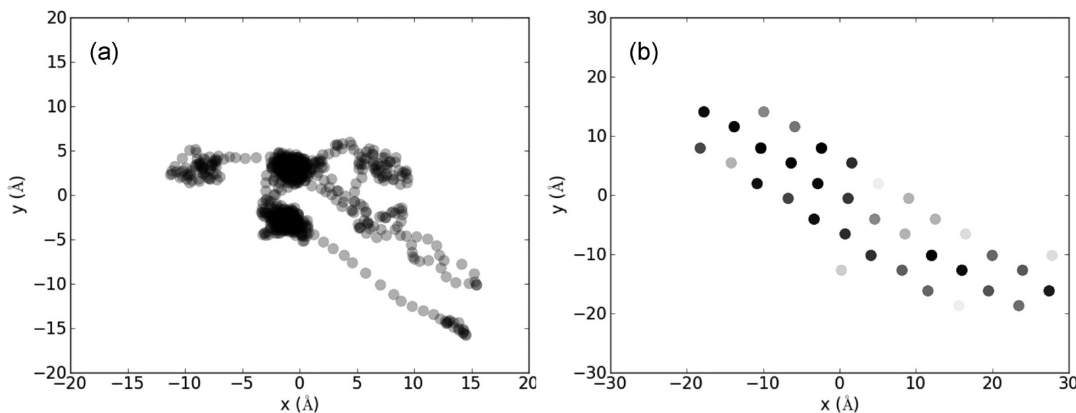


**Figure 7.**  $C_{60}$  center-of-mass trajectories on bulk phase pentacene using (a) MD and (b) kinetic Monte Carlo. Each simulation was performed for 1 ns at 300 K.

simulation of a single  $C_{60}$  molecule diffusing over bulk phase pentacene.<sup>2</sup> Figure 7 compares the trajectories of one  $C_{60}$  molecule diffusing on a bulk phase pentacene surface using MD and KMC, each for 1 ns at 300 K. From the figure, it is evident that the KMC code captures the anisotropy of the  $C_{60}$  molecule on bulk phase pentacene as well as the lateral extent of diffusion that occurs in 1 ns. For a more quantitative comparison, we calculated the diffusion coefficient of  $C_{60}$  on bulk phase pentacene using KMC and compared it to that already obtained using MD.<sup>2</sup> As shown in Figure 8, the KMC simulations

distance apart) of the initial and final position were considered for simplicity. In calculating the energy barriers, we averaged the effect of rotational degrees of freedom to minimize any spurious effects of  $C_{60}$  facets on energy barriers. Figure S3, Supporting Information, shows schematics of all the unique arrangements of (near)  $C_{60}$  molecules on a Hex lattice along with their corresponding energy barriers. In the end, we categorized these arrangements by three factors that determined the energy barrier: the number of initial neighbors, the number of final neighbors, and how many shared neighbors exist between the initial and final jump sites (this can be zero, one, or two).

**3.4. Hex-Bulk Jump Rates.** The energy barriers for Hex-bulk jumps depend not only on the number of initial and final neighbors (as in the case for the Hex-sub jumps described previously) but also on the proximity of the diffusing  $C_{60}$  molecule to the edge of the island below it (see Figure 9). When the

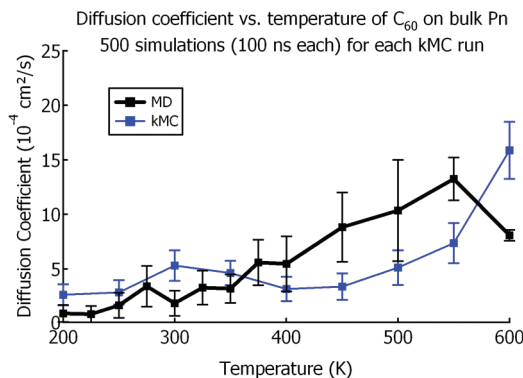


**Figure 8.**  $C_{60}$  diffusion coefficients on bulk phase pentacene vs temperature using MD and KMC.

reproduce the MD-derived diffusion coefficients within a factor of about 5 or less; diffusion coefficients reproduced within an order of magnitude can be regarded as satisfactory. The KMC simulation overestimates the diffusion coefficient at very high temperatures because it does not take into account the effect of the enhanced movement of the pentacene surface disrupting the  $C_{60}$  diffusion. We have seen this in MD, but it is too complex and stochastic to capture in the KMC code. Overall, however, the Q–P lattice system in the KMC simulations correctly predicts the behavior of solitary diffusing  $C_{60}$  molecules, both qualitatively and quantitatively.

**3.3. Hex-Sub Jump Rates.** To obtain rates for Hex-sub jumps, it was infeasible to perform multiple MD simulations at different temperatures as it had been for the QP jump rates. This is mainly because additional  $C_{60}$  molecules add significantly to computational expense. Instead, we calculated static energy barriers using molecular mechanics. Only “near” neighbors (defined as neighbors exactly one  $C_{60}$  van der Waals

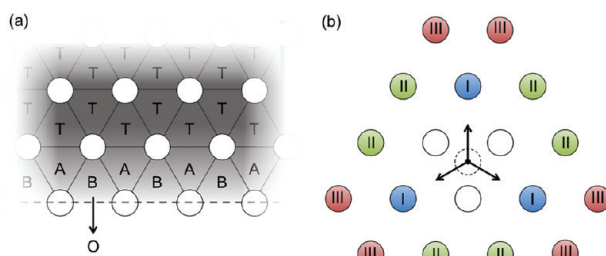


**Figure 9.** Schematics to describe  $C_{60}$  islands and near-edge sites. In both (a) and (b), circles represent possible positions of  $C_{60}$  molecules in a  $C_{60}$  island (diameters are under-represented for clarity); circles outlined in solid black represent molecules in one plane (i.e., within the same monolayer), and the dotted circle in (b) is a molecule atop that monolayer. (a) The three different site types (A, B, T) designate the proximity of a site to an island edge (dotted line), and the O site designates that a molecule has fallen over the edge of an island. (b)  $C_{60}$  occupation at sites labeled I (blue), II (green), and III (red) is used to determine how close the jumping molecule (dotted circle) is to the edge of an island.

diffusing molecule is far from the edge, i.e., on a terrace, the energy barrier toward an edge is lower than that when it is close to an edge, since the existence of a Schowbel barrier typically retards diffusion over the edge of an island. After testing energy barriers of different island sizes, it was determined that  $C_{60}$  jumps starting from positions beyond the second  $C_{60}$  row from the edge were essentially identical to those in the middle of a

terrace (no proximity to a step). Figure 9a shows the different types of sites considered near edges. A “T” site refers to a jump starting from a terrace (a site away from, uninfluenced by, a  $C_{60}$  island edge), and “A” and “B” sites refer to jumps starting at a  $C_{60}$  island edge where only “B” jumps can result in  $C_{60}$  molecules falling over the edge of the island, surmounting a Schwoebel barrier.

In general,  $C_{60}$  jumps that move toward the edge of a  $C_{60}$  island have a higher energy barrier than  $C_{60}$  jumps far from an edge, confirming the existence of a Schwoebel barrier.<sup>20</sup> In the KMC code, this distinction was taken into consideration in detail. Figure 9b classifies the types of sites considered in determining the energy barrier of a particular jump. The presence of type-I sites (blue) determines whether or not the molecule starts out at a “B” site and, if so, whether the jump would result in the molecule going over the edge (referred to as an “O” event to designate “over”); the presence of type-II sites (green) determines whether or not the molecule starts out at an “A” site and/or ends up at a “B” site. The presence of type-III sites (red) determines whether a jump results in an “A” site or a “T” (terrace) site. Thus, a Hex-bulk jump will take place either as T-to-T (or A), A-to-T, A-to-B, B-to-O, or B-to-A, each of which has a unique set of energy barriers depending on the number of initial and final neighbors. Figure S4, Supporting Information, catalogues each of these energy barriers for reference. Of these energy barriers, the B-to-O are highest because these correspond to Schwoebel barriers to surmount a  $C_{60}$  step edge. The A-to-T and B-to-A energy barriers are the lowest because these are favorable jumps away from the  $C_{60}$  edge.

**3.5. Comparison to Past Work.** At this point, it is appropriate to compare the library of energy barriers generated in this study to those quoted in a paper by Liu et al. because this is the only other occurrence in the literature where a KMC simulation of  $C_{60}$  growth on  $C_{60}$  has been performed.<sup>21</sup> Liu et al. found fractal-dendritic growth of second-layer  $C_{60}$  islands on compact first-layer  $C_{60}$  islands deposited on graphite substrate. Their island morphologies agreed well with STM images taken under comparable experimental conditions. There are a few differences between our system and theirs: Liu et al. studied  $C_{60}$  growth on perfectly compact first-layer  $C_{60}$  islands, whereas we are studying  $C_{60}$  growth on pentacene with multilayer  $C_{60}$  island formation. Also, they considered two  $C_{60}$  monolayers on graphene, where the presence of the graphene might influence the diffusion of second-layer  $C_{60}$  molecules differently than pentacene. These differences make comparing morphological results for growth processes inappropriate, but it is still worth noting the differences in rates and energy barriers.

There are also some differences in methodology, which could also contribute to any discrepancies. Liu et al. used a coarse-grained Girifalco potential to run dynamic simulations, from which jump rates were calculated. The energy barriers quoted from Liu et al. were obtained by fitting the jump rates to an Arrhenius equation. On the other hand, our energy barriers were obtained from static energy calculations from an all-atom semiempirical model (MM3). Figures 10 and 11 compare the Liu et al. energy barriers with those reported by us. Liu et al. needed fewer values than we did (see Figure S4, Supporting Information), so we only compare this set. A few of the energy barriers, like those shown in Figure 10a,b are very close in value, but overall, the energy barriers they obtained are consistently lower than in this study by about 0.1 eV (approximately  $4 k_B T$  at room temperature), which is significant. In the Liu et al. paper, some jump types with “far” neighbors (distanced by  $2\sqrt{3}/3$  times

		Molecular Mechanics-derived using MM3	MD-derived from Liu et al. paper
(a)	I	$E_a = 0.205 \pm 0.022$ eV	$E_a = 0.178 \pm 0.004$ eV $v_0 = 2 \times 10^{11} \text{ s}^{-1}$
	II	“ “	“ “
	III	“ “	“ “
(b)	I	$E_a = 0.448 \pm 0.025$ eV	$E_a = 0.429 \pm 0.057$ eV $v_0 = 6.5 \times 10^{11} \text{ s}^{-1}$
	II	$E_a = 0.289 \pm 0.029$ eV	$E_a = 0.185 \pm 0.006$ eV $v_0 = 2.5 \times 10^{11} \text{ s}^{-1}$
	III	N/A	N/A
(c)	I	$E_a = 0.295 \pm 0.024$ eV	P=0%
	II	$E_a = 0.111 \pm 0.021$ eV	P=50%
	III	“ “	P=50%
(d)	I	$E_a = 0.717 \pm 0.029$ eV	$E_a = \infty$
	II	N/A	N/A
	III	N/A	N/A
(e)	I	$E_a = 0.556 \pm 0.028$ eV	$E_a = 0.354 \pm 0.063$ eV $v_0 = 6 \times 10^{10} \text{ s}^{-1}$
	II	“ “	“ “
	III	N/A	N/A
(f)	I	$E_a = 0.054 \pm 0.023$ eV	P=98.24%
	II	$E_a = 0.189 \pm 0.024$ eV	P=0.88%
	III	“ “	“ “
(g)	I	$E_a = 0.337 \pm 0.025$ eV	$E_a = \infty$
	II	$E_a = 0.385 \pm 0.031$ eV	$E_a = \infty$
	III	N/A	$E_a = \infty$
(h)	I	$E_a = 0.344 \pm 0.028$ eV	P=99.86%
	II	$E_a = 0.180 \pm 0.026$ eV	P=0.14%
	III	N/A	N/A
(i)	I	$E_a = 0.418 \pm 0.036$ eV	$E_a = \infty$
	II	N/A	N/A
	III	N/A	N/A

**Figure 10.** Comparison of terrace energy barriers ( $E_a$ ) of  $C_{60}$  on  $C_{60}$  obtained by the method described in this work (molecular mechanics) and the method of Liu et al. (MD).<sup>21</sup> Liu et al. also provided attempt frequencies ( $v_0$ ) for certain jump types. They provide probabilities ( $P$ ) for jump types, where they quote the initial configuration as a metastable state.

the van der Waals diameter), like those shown in Figure 10c,f, are reported as probabilities in lieu of quoting energy barriers. Their rationale is that the initial configuration in these situations is a metastable state (i.e., the jump rate is higher than that of a jump with no neighbors), so if this situation presents itself, a jump will automatically be performed with a certain probability. We think that there are some cases where this may not hold. For example, in Figure 10h, we calculate an energy barrier for jump I of 0.34 eV, which is higher than that of a basic neighborless jump (0.21 eV as shown in Figure 10a). Liu et al. assume that this initial state is metastable and has a 99.86% probability of jumping. There are also some situations where they state an infinite energy barrier, yet we find that there is only a moderate (potentially surmountable) energy barrier. Jump I in Figure 10g is an example of this, where

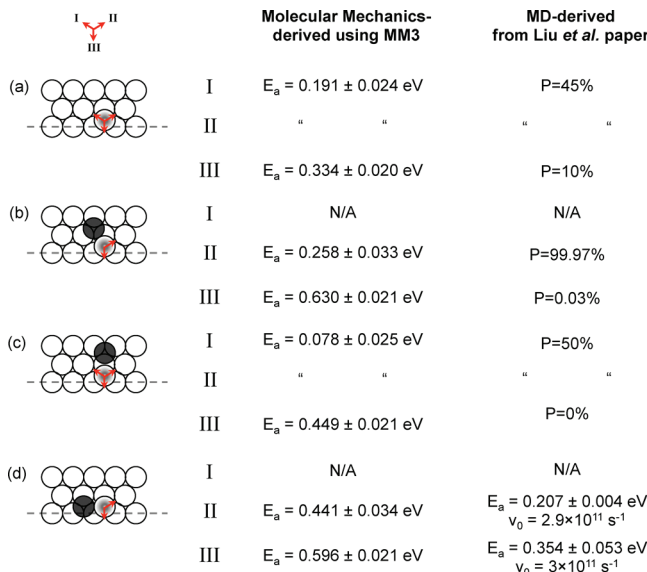


Figure 11. Comparison of energy barriers at a  $C_{60}$  step edge. Key as in Figure 10.

we calculate an energy barrier of 0.34 eV and Liu et al. describe this barrier as infinite.

#### 4. SENSITIVITY ANALYSIS OF KEY PARAMETERS

In our submonolayer studies, we consider the sensitivity of the system behavior to changing the Hex prefactor and deposition rate, since the choice of these two parameters strongly affects how long the simulation takes to execute. The lower the deposition rate, the greater the disparity between the deposition rate and the rate of diffusion events and the more rate limiting these diffusion events become. The larger the Hex prefactor, the faster the diffusion events become and the more rate limiting they become. Thus, the combination of a small Hex prefactor and a high deposition rate gives the fastest completion. Figure 12 shows the CPU time taken in days for different combinations of Hex prefactor and deposition rate.

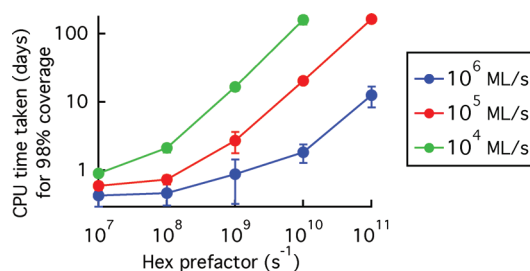


Figure 12. CPU time taken in days for monolayer coverage to reach 95% as a function of Hex prefactor and deposition rate.

The deposition rate was varied from  $10^4$ – $10^6$  ML/s, and the Hex prefactor was varied from  $10^7$ – $10^{11}$   $\text{s}^{-1}$ . For our  $71 \times 89$  unit cell bulk pentacene system size,  $10^4$  ML/s corresponds to a deposition rate of  $\sim 10^7 \text{ s}^{-1}$  (depositions per second),  $10^5$  ML/s to  $\sim 10^8 \text{ s}^{-1}$ , and  $10^6$  ML/s to  $\sim 10^9 \text{ s}^{-1}$ . A “realistic” deposition rate would be about 1 ML/s ( $\sim 10^3 \text{ s}^{-1}$ ) but because this rate is much slower than the rate of diffusion events ( $\sim 10^{10} \text{ s}^{-1}$ ), the simulation would evolve in time extremely slowly. The range of Hex prefactors overlaps the range of previously reported values for attempt frequencies of the diffusion of large molecules,

$10^{10}$ – $10^{14}$   $\text{s}^{-1}$ , such as 4-*trans*-2-(pyrid-4-yl-vinyl) benzoic acid (PVBA), decacyclene (DC), hexa-*tert*-butyl-decacyclene (HtBDC), and  $C_{60}$ .<sup>21–24</sup> In particular,  $C_{60}$  on Pd(110) with surface traps has a reported prefactor of  $10^{14} \text{ s}^{-1}$  (found experimentally),<sup>24</sup> and  $C_{60}$  on  $C_{60}$  has a reported prefactor of  $6 \times 10^{10}$ – $6.5 \times 10^{11} \text{ s}^{-1}$  (found from MD simulations).<sup>21</sup> Lastly, for comparison, the average of the QP jump prefactors obtained here from MD simulations of a single  $C_{60}$  molecule diffusing over a pentacene surface was  $1.18 \times 10^{11}$ . From this information, we can assume that the Hex prefactor should be in the range of  $O(10^{10})$ – $O(10^{11}) \text{ s}^{-1}$ .

Before picking the smallest Hex prefactor and the highest deposition rate for convenience, we must determine the sensitivity of the system’s properties to choices of these parameters. As a metric for system behavior, we chose the cluster size distribution at 10% coverage. Figure 13 shows both

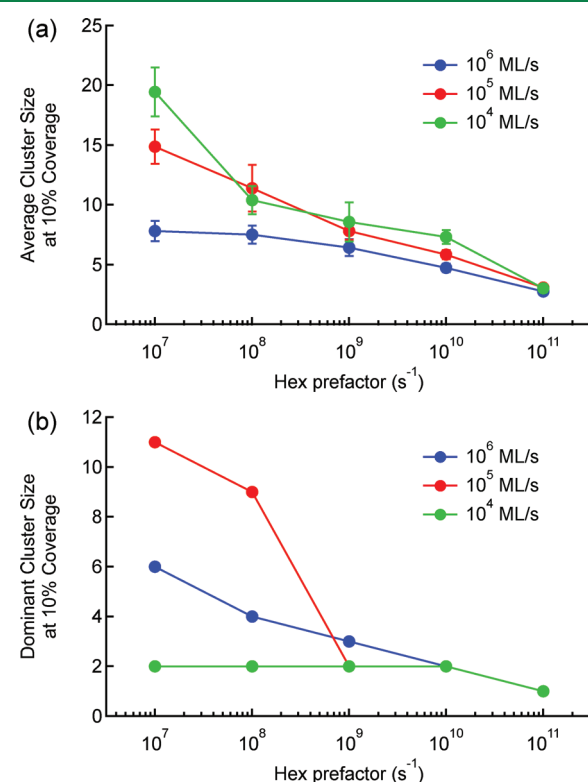
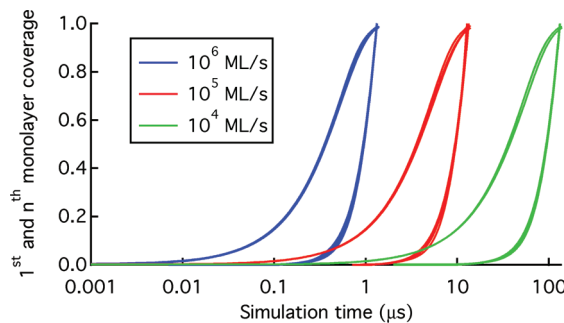


Figure 13. (a) Average and (b) dominant cluster sizes at 10% coverage as a function of Hex prefactor and deposition rate. These values were taken from histogram distributions, each containing the statistics of 10 different simulations.

the average and dominant (i.e., most probable) cluster sizes at 10% coverage for different Hex prefactors and deposition rates. The deposition rate curves converge around Hex prefactors of  $10^{10}$ – $10^{11} \text{ s}^{-1}$ . Hex prefactors lower than this show significantly different behavior for different deposition rates. Thus, if we stay within the Hex prefactor range of  $10^{10}$ – $10^{11} \text{ s}^{-1}$ , raising the deposition rate at most to  $10^6$  ML/s will not significantly alter the system behavior.

We also considered a second metric regarding the sensitivity analysis, namely the evolution of submonolayer and beyond monolayer coverage as a function of simulation time. Figure 14 shows the first and  $n^{\text{th}}$  monolayer coverage as a function of simulation time and deposition rate. This figure plots curves for the different Hex prefactors; they overlap each other within



**Figure 14.** First (left side) and  $n^{\text{th}}$  (right side) fractional monolayer coverage as a function of simulation time for different deposition rates. Results for different Hex prefactors are indistinguishable on this scale.

each set of deposition rate data, and cannot be seen. Thus, there is a negligible effect of the Hex prefactor on the rate of coverage. It might be thought, since a lower hex prefactor yields fewer larger clusters, that submonolayer growth would be slower due to the higher tendency of a molecule to land on top of an already clustered island. Magnification of this graph shows that this is the case, but the effect is negligible. Note that for  $10^4$  ML/s, near 100% coverage occurs at  $\sim 0.1$  ms.

The  $n^{\text{th}}$  monolayer curves in Figure 14 (right side within each deposition rate data set) do not reach a plateau like the submonolayer curves because this  $n^{\text{th}}$  monolayer curve represents the sum of the second ML, third ML, etc., each of which would plateau like the first layer. These data were taken from an earlier version of the KMC code, where there is no interlayer diffusion and second and third monolayer molecules can occupy the same space upon deposition (obviously impossible). This was the main motivation for incorporating interlayer diffusion into the KMC simulation method. Despite this, the lower portion of the  $n^{\text{th}}$  layer curves should still accurately represent the system behavior, before interlayer diffusion can play any significant role. For each deposition rate tested, when the second monolayer reaches 5% coverage (small enough to be considered initial stages, but large enough to be compared to experiments), the first monolayer has already completed  $\sim 50\%$  coverage. Regarding the sensitivity of

coverage to Hex prefactor and deposition rate, we conclude that the choice of hex prefactor does not significantly affect the coverage evolution and that the deposition rate merely affects the rate of coverage, as would be expected.

## 5. KMC SIMULATIONS OF SUBMONOLAYER OF $C_{60}$ DEPOSITION

Initially, the code was written for submonolayer  $C_{60}$  growth, where if a molecule is deposited on top of a  $C_{60}$  island, it fixes in place those molecules directly underneath but is otherwise ignored. This approach is the focus of this section, while further development of the multilayer code will be discussed at the end. The submonolayer approach was used in Section 4 for the sensitivity analysis concerning  $C_{60}$  growth behavior at 10% coverage. The submonolayer growth is perhaps best represented by a physical picture of the thin film, showing island shapes as well as sizes. Figure 15 shows snapshots of 10, 20, 30, 40, and 50% coverage for  $C_{60}$  growth on both thin film and bulk phase pentacene. Both simulations were performed at 300 K,  $10^6$  ML/s, and a Hex prefactor of  $10^{10}$  s $^{-1}$ . There appears to be a tendency for islands to grow diagonally in the [110] direction on the bulk phase; however, we believe this might be an artifact of slightly unequal jump rates in opposite directions, which occurs from averaging out the stochastic nature of MD-derived jump rates (see Figures S1 and S2, Supporting Information). This detail is important over long times because it leads to the constraint of “detailed balance” not being satisfied. Nonetheless, this artifact of anisotropic island shapes is much less pronounced on the thin film phase, where the nature of the jump rates is inherently more isotropic.<sup>2</sup> Thus, the effect of multiple lattices for heteroepitactical growth can clearly be seen here for  $C_{60}$  on bulk phase pentacene. Interpreting these submonolayer results further was precluded by the need to develop the multilayer code and obtain experimental images and growth data of the  $C_{60}$ /pentacene systems in question.

The addition of multiple layers in the KMC code introduces a greater number of possible events and necessitates a more complicated method of handling deposition. The deposition method for the multiple-layer code involves determining

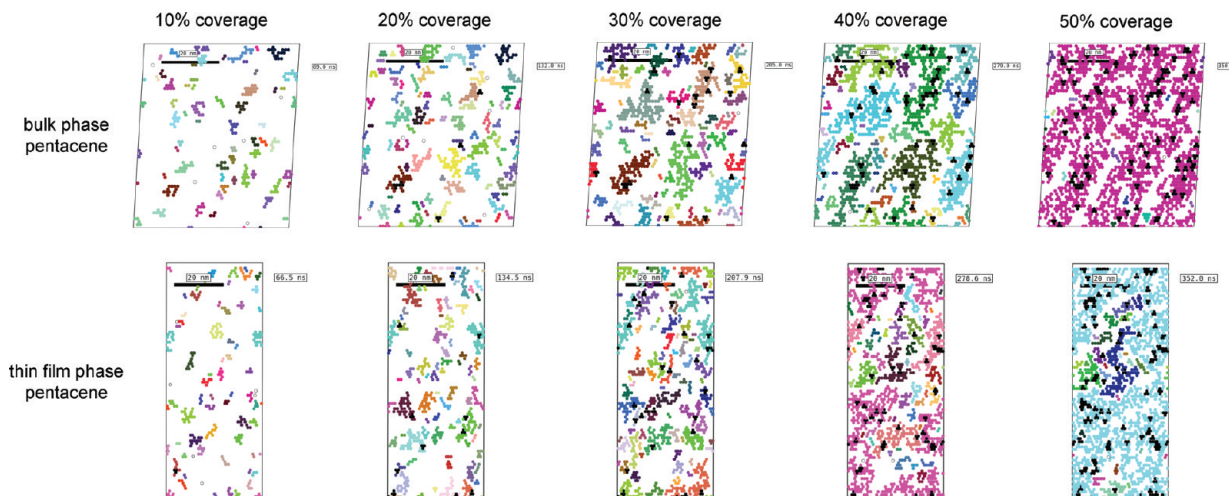


**Figure 15.** Snapshots of  $C_{60}$  submonolayer growth on bulk phase (top) and thin film phase (bottom) upright pentacene phases. Both simulations were performed at 300 K,  $10^6$  ML/s, and with a Hex prefactor of  $10^{10}$  s $^{-1}$ . The different colors represent separate clusters, and the black colors represent  $C_{60}$  molecules that have been landed upon during a subsequent deposition event and are then deemed to be “frozen” in place. The black bar represents a length scale of 20 nm.

whether a C<sub>60</sub> molecule is deposited onto a C<sub>60</sub> triangle or not (see Figure 3b). Previously, we had assumed that if a molecule was deposited on such a triangle, those triangle molecules were not allowed to move (shown as black particles in Figure 15), and the deposited molecule was ignored. In the multiple layer version of the KMC code, no molecule is ignored. The multilayer simulations are preliminary at the moment and are only mentioned here for completeness because the focus of the paper is method development for heteroepitactical growth.

## 6. CONCLUSIONS

We have presented a multilattice framework for a KMC algorithm with grid-switching capabilities. This was needed to capture the unique surface terrain that the herringbone structure of upright pentacene provides. In the process of creating the model, we also gained useful information from the large set of energy barriers. The energy barrier data shown in Figures S1 and S2, Supporting Information, are the most comprehensive sets that exist for C<sub>60</sub> on pentacene and C<sub>60</sub>-on-C<sub>60</sub>, and compare well with the energy barriers that already exist in the literature. The C<sub>60</sub>-on-C<sub>60</sub> energy barriers from the Liu et al. paper<sup>21</sup> overlap quite well with the ones we obtained. Our studies also confirmed the result by Goose et al., who found the minimum value for the Erhlich–Schwoebel barrier for C<sub>60</sub>-on-C<sub>60</sub> to be ~0.31 eV,<sup>20</sup> which is very close to the value determined here (0.33 eV). By implementing this KMC method, we were able to simulate microseconds of time and tens of nanometers, scales unattainable by MD methods. Even so, the detailed differences between the behavior of C<sub>60</sub> on thin film and bulk phase pentacene deterministically described by MD were able to be captured in KMC.

Jump rates for C<sub>60</sub> on pentacene, obtained in this work, are system-specific, but this approach can be more broadly applied. The multilattice KMC code developed in this work could be applied to other oblique-hexagonal lattice systems for heteroepitactical growth. Organic substrates with herringbone-type packing (e.g., anthracene, tetracene, napthalene, rubrene) are very common; accommodating these materials would be a very easy extension to this code. This would entail obtaining jump rates either by molecular mechanics or MD methods as described in Section 3.

Returning to the C<sub>60</sub>/pentacene system, it would be helpful to have experimental growth data to validate subsequent KMC simulations of the nature presented here. For example, such data could validate the predictions we have made of the point at which the first, second, and third monolayers begin to grow. Several future studies could use the algorithm presented here: First, it would be valuable to compare multilayer C<sub>60</sub> island morphologies on a perfectly compact first layer to those obtained by Liu et al., who found fractal C<sub>60</sub> island formation on a C<sub>60</sub> substrate. Second, simulating defects, vacancies, or substrate step edges would give insight into the behavior of C<sub>60</sub> growth in nonideal conditions. In the longer term, implementing an off-lattice KMC approach would be worthwhile to facilitate capturing diffusion at island edges, which would fine-tune the prediction of microstructural evolution and increase the computational efficiency. However, the development of an off-lattice KMC approach or  $\tau$ -leaping algorithms to accelerate the code will not be straightforward.

## ■ ASSOCIATED CONTENT

### S Supporting Information

This material contains the Arrhenius plots for all C<sub>60</sub>-on-pentacene Q–P jump combinations as well as the static energy barrier calculations for the C<sub>60</sub>-on-C<sub>60</sub> jump possibilities. These data were necessary in order to obtain jump rates for the KMC algorithm. This material is available free of charge via the Internet at <http://pubs.acs.org/>.

## ■ AUTHOR INFORMATION

### Corresponding Author

\*E-mail: paulette.clancy@cornell.edu.

### Notes

The authors declare no competing financial interest.

## ■ ACKNOWLEDGMENTS

The authors acknowledge funding from the National Science Foundation funded MRSEC administered by Cornell's Center for Materials Research (CCMR) for R.A.C.'s financial support.

## ■ REFERENCES

- (1) Cantrell, R.; Clancy, P. *Surf. Sci.* **2008**, *602*, 3499–3505.
- (2) Cantrell, R.; Clancy, P. *Mol. Simul.* **2010**, *36*, 590–603.
- (3) Cantrell, R. A.; Clancy, P. *Mater. Res. Soc. Symp. Proc.* **2010**, *1263*, 1263-Y05-06.
- (4) Cantrell, R. A.; James, C.; Clancy, P. *Langmuir* **2011**, *27*, 9944–9954.
- (5) Yi, Y.; Coropceanu, V.; Brédas, J.-L. *J. Am. Chem. Soc.* **2009**, *131*, 15777–15783.
- (6) Miron, R. A.; Fichthorn, K. A. *J. Chem. Phys.* **2003**, *119*, 6210–6216.
- (7) Voter, A. F. *J. Chem. Phys.* **1997**, *106*, 4665–4677.
- (8) Steiner, M. M.; Genilloud, P.-A.; Wilkins, J. W. *Phys. Rev. B* **1998**, *57*, 10236–10239.
- (9) Wang, J.-C.; Pal, S.; Fichthorn, K. A. *Phys. Rev. B* **2001**, *63*, 085403.
- (10) Itoh, M.; Bell, G. R.; Joyce, B. A.; Vvedensky, D. D. *Surf. Sci.* **2000**, *464*, 200–210.
- (11) Bogicevic, A.; Strömquist, J.; Lundqvist, B. I. *Phys. Rev. Lett.* **1998**, *81*, 637–640.
- (12) Köhler, U.; Jensen, C.; Wolf, C.; Schindler, A. C.; Brendel, L.; Wolf, D. E. *Surf. Sci.* **2000**, *454*–456, 676–680.
- (13) Fichthorn, K. A.; Scheffler, M. *Phys. Rev. Lett.* **2000**, *84*, 5371–5374.
- (14) Chatterjee, A.; Vlachos, D. G. *Chem. Eng. Sci.* **2007**, *62*, 4852–4863.
- (15) Baskaran, A.; Devita, J.; Smereka, P. *Continuum Mech. Thermodyn.* **2010**, *22*, 1–26.
- (16) Hoffmann, M. J. CO Oxidation on Palladium Using Multi-lattice Kinetic Monte Carlo. *Ph.D.*; Freie Universität Berlin: Berlin, Germany, 2010.
- (17) Pacheco, J. M.; Ramalho, J. P. *Phys. Rev. Lett.* **1997**, *79*, 3873.
- (18) Yamamoto, M.; Fujinami, A.; Ogata, S.; Shibutani, Y. *J. Comput. Sci. Technol.* **2007**, *1*, 14–21.
- (19) Zoonjens, P.; Grochola, G.; Snook, I. K.; Russo, S. P. *J. Phys.: Condens. Matter* **2011**, *23*, 015302.
- (20) Goose, J. E.; First, E. L.; Clancy, P. *Phys. Rev. B* **2010**, *81*, 205310.
- (21) Liu, H.; Lin, Z.; Zhigilei, L. V.; Reinke, P. *J. Phys. Chem. C* **2008**, *112*, 4687–4695.
- (22) Schunack, M.; Linderoth, T.; Rosei, F.; Lægsgaard, E.; Stensgaard, I.; Besenbacher, F. *Phys. Rev. Lett.* **2002**, *88*, 156102.
- (23) Weckesser, J.; Barth, J. V.; Kern, K. *J. Chem. Phys.* **1999**, *110*, 5351–5354.
- (24) Weckesser, J.; Barth, J. V.; Kern, K. *Phys. Rev. B* **2001**, *64*, 161403.